

Multispectral imaging for quantitative and compartment-specific immune infiltrates reveals distinct immune profiles that classify lung cancer patients

Artur Mezheyeuski^{1*}, Christian Holst Bergsland², Max Backman¹, Dijana Djureinovic¹, Tobias Sjöblom¹, Jarle Bruun² and Patrick Mücke¹

¹ Department of Immunology, Genetics and Pathology, Uppsala University, Uppsala, Sweden

² Department of Molecular Oncology, Institute for Cancer Research, the Norwegian Radium Hospital, Oslo University Hospital, Oslo, Norway

*Correspondence to: A Mezheyeuski, Rudbeck Laboratory, Department of Immunology, Genetics and Pathology, Uppsala University, 751 83 Uppsala, Sweden. E-mail: artur.mezh@gmail.com

Abstract

Semiquantitative assessment of immune markers by immunohistochemistry (IHC) has significant limitations for describing the diversity of the immune response in cancer. Therefore, we evaluated a fluorescence-based multiplexed immunohistochemical method in combination with a multispectral imaging system to quantify immune infiltrates *in situ* in the environment of non-small-cell lung cancer (NSCLC). A tissue microarray including 57 NSCLC cases was stained with antibodies against CD8, CD20, CD4, FOXP3, CD45RO, and pan-cytokeratin, and immune cells were quantified in epithelial and stromal compartments. The results were compared with those of conventional IHC, and related to corresponding RNA-sequencing (RNAseq) expression values. We found a strong correlation between the visual and digital quantification of lymphocytes for CD45RO (correlation coefficient: $r = 0.52$), FOXP3 ($r = 0.87$), CD4 ($r = 0.79$), CD20 ($r = 0.81$) and CD8 ($r = 0.90$) cells. The correlation with RNAseq data for digital quantification (0.35–0.65) was comparable to or better than that for visual quantification (0.38–0.58). Combination of the signals of the five immune markers enabled further subpopulations of lymphocytes to be identified and localized. The specific pattern of immune cell infiltration based either on the spatial distribution (distance between regulatory CD8⁺ T and cancer cells) or the relationships of lymphocyte subclasses with each other (e.g. cytotoxic/regulatory cell ratio) were associated with patient prognosis. In conclusion, the fluorescence multiplexed immunohistochemical method, based on only one tissue section, provided reliable quantification and localization of immune cells in cancer tissue. The application of this technique to clinical biopsies can provide a basic characterization of immune infiltrates to guide clinical decisions in the era of immunotherapy.

Copyright © 2017 Pathological Society of Great Britain and Ireland. Published by John Wiley & Sons, Ltd.

Keywords: digital pathology; tumour microenvironment; checkpoint therapy; deep-learning microscopy; prognosis; PD-L1

Received 10 October 2017; Revised 7 November 2017; Accepted 13 December 2017

No conflicts of interest were declared.

Introduction

The introduction of immunotherapy, namely inhibitors against cytotoxic T-lymphocyte-associated protein 4 and programmed death 1/programmed death ligand 1 (PD-L1), has revolutionized the treatment of many solid tumours, including melanoma, lung, bladder cancer and head and neck cancer [1–5]. Although remarkable disease control rates are observed in many patients with previous failure of standard therapy, durable response or cure is obtained in only a minority of patients [6,7]. The reason for primary resistance and secondary resistance against checkpoint blockade are only poorly understood [8,9], and currently only PD-L1 expression serves as a predictive biomarker in some of the indications [10–12]. However, the performance of this predictive test is limited, and many technical issues and subjective

aspects of interpretation have hampered clinical use [13]. Thus, extensive efforts are ongoing to better understand the immune response in cancer, in order to find better predictive biomarkers or alternative immune targets for treatment [14].

There is evidence that the immune reaction in the primary tumour as such has a significant impact on the course of the disease even without any immune-modulating therapy [15–22]. One of the most acknowledged contributions has been the work of the Galon group, who established the Immunoscore in colorectal cancer, based on the location, amount and type of the immune cells; this is a stronger predictor of patients survival than microsatellite instability (MSI). MSI is the pan-cancer biomarker for immunotherapy, but Galon *et al* also suggested that a subgroup among microsatellite-stable cancers may benefit from

immunotherapy based on a high Immunoscore [23,24]. Immune classifiers using careful annotations of immune cells were also able to predict the benefit of adjuvant chemotherapy in various cancer types [11,25–27]. Not surprisingly, many association studies of specific immune cell compositions and the response to checkpoint inhibitors have been performed [28,29]. Much work has also been invested in lung cancer, for which checkpoint inhibition is already approved for first-line and second-line treatment of advanced non-small-cell lung cancer (NSCLC) patients. Indeed, high numbers of CD8⁺ lymphocytes infiltrating the cancer cell compartment showed a significant association with response to checkpoint inhibition in NSCLC patients and those with other cancer types [30]. Thus, the immune cell context of cancer may also have direct clinical implications for prognosis and choice of therapy.

The assessment of immune cells or immune markers is traditionally performed by pathologists annotating immunohistochemical staining of cancer tissue with lymphocyte-specific markers, e.g. CD4, CD8, and FOXP3. Advantages of this technique are its relatively low cost and the fact that immune cells can be annotated with regard to their location in the stromal or tumour compartment. This method is, however, relatively time-consuming, and is dependent on the experience of the observer [13,31]. Semiquantitative assessment provides only crude estimations of immune cell counts. Furthermore, different cell types must be annotated in consecutive tissue sections, making it difficult to relate cells to each other. The same issue limits also the subclassification of immune cells with two or more markers, e.g. CD4⁺FOXP3⁺ cells.

For clinical lung cancer specimens, the situation is complicated because the amount of tissue available is most often limited to minimal tissue biopsies. The diagnostic algorithm with selected immunostains (thyroid transcription factor 1; p40) for accurate cancer diagnosis [32], anaplastic lymphoma kinase immunohistochemistry (IHC) [33] and eventually molecular mutation testing is tissue-demanding. Hence, basic characterization of the immune cell composition of each tissue biopsy for research, as a companion diagnostic in clinical trials or in routine diagnostics is unrealistic.

To tackle the disadvantages of IHC, while retaining histological resolution for cell annotation, we used a multispectral image system that, in combination with a multiplexed fluorescence immunohistochemical technique, can localize and quantify immune cells in diagnostic tissue specimens. The aim of this study was to compare this approach with conventional visual assessment of immune cells by use of an extensively annotated tissue microarray (TMA) of 57 lung cancer patients to correlate immune cell counts from consecutive tissue sections. Furthermore, distance mapping of immune cells was performed, and immune signatures were related to clinical parameters.

Materials and methods

Patient cohort and TMAs

TMAs were constructed from tissues obtained from surgically resected NSCLC patients operated on between 2006 and 2010 at the Uppsala University Hospital. Tissues from 60 patients were included in this TMA, with two 1-mm-diameter cores for each case, as described previously [13]. Clinical and pathological data of the 57 patients with evaluable tissue cores that were finally used for the analysis are provided in supplementary material, Table S1. RNA sequencing (RNAseq) data were available for 35 patients, as previously described [34]. The study was approved by the Uppsala Ethical Review Board (reference 2012/532).

RNA sequencing

RNAseq analysis was performed as described previously [34]. RNA was extracted from frozen tissue samples with >10% tumour cell content. Samples were prepared by use of the Illumina TruSeq RNA Sample Prep Kit v2 (Illumina, San Diego, CA, USA), with polyA selection. The sequencing was performed multiplexed with five samples per lane on Illumina HiSeq2500 machines (Illumina), by use of the standard Illumina RNAseq protocol with a read length of 2 × 100 bases. The raw sequencing data were mapped to the human reference genome (GRCh37) and the Ensembl version 73 gene annotation by the use of TopHat version 2.0.8b [35,36]. Gene fragments per kilobase of transcript per million mapped reads values were calculated from the generated alignments by the use of Cufflinks version 2.1.1. Raw read counts were calculated with featureCounts from the Subread package version 1.4.0-p1 [37]. The raw sequencing data have been deposited at <http://www.ncbi.nlm.nih.gov/geo/>, with the accession number GSE81089.

Conventional immunohistochemical staining

Sections of thickness 4 µm were heated to 50 °C for 12 h, deparaffinized, and rehydrated. Blocking of endogenous peroxidase was accomplished by a 5-min exposure to 0.3% H₂O₂ in 95% ethanol. Heat-induced epitope retrieval was used as the antigen retrieval method, with 4 min of pressure boiling with a pH 6 retrieval buffer and subsequent cooling to 90 °C. A full protocol can be found at the website of the human protein atlas (http://www.proteinatlas.org/download/IHC_protocol.pdf).

Immunohistochemical analysis was performed with monoclonal anti-human mouse antibodies: anti-CD4 (Atlas Antibodies, Bromma, Sweden; AMAb90754; 1:125), anti-CD8A (Atlas Antibodies; AMAb90883; 1:250), anti-CD20 (Dako; Agilent Technologies, Santa Clara, CA, USA; IR604; ready-to-use dilution), anti-FOXP3 (Santa Cruz Biotechnology, Santa Cruz, CA, USA; sc-56680; 1:15) and anti-CD45RO (Abcam, Cambridge, UK; ab86080; 1:1000).

Visual scoring

Scoring of immune cell infiltrates was performed semi-quantitatively by microscopic inspection. Scores were taken as percentage of stained viable nucleated cells in the stromal and tumour compartments respectively. Cut-offs were as follows: 1%, 5%, and further 5% increments up to 40%, and then 10% increments up to 100%. Scoring was performed by M.B. and supervised by a consultant pathologist (P.M.).

Multimarker immunohistochemical staining

Multiplexed immunohistochemical staining was performed with the Opal 7 Tumor Infiltrating Lymphocyte Kit according to the manufacturer's instructions (PerkinElmer, Waltham, MA, USA), except for pan-cytokeratin staining (discussed below). This protocol was based on the use of fluorescent TSA reagents, which allows for microwave treatment to remove primary and secondary antibodies, while retaining an intact fluorescent signal [38]. This process is repeated until all antigens have been stained with their respective fluorophores.

The antibodies were diluted as follows: anti-CD4, 1:50; anti-CD8, 1:800; anti-CD20, 1:1500; anti-FOXP3, 1:600; and anti-CD45RO, 1:150. We used a separate combination of epithelial markers (Blom *et al*, submitted) to visualize the epithelial tissue instead of the pan-cytokeratin provided in the kit, as we have observed that this provides better delineation of the tissue. This combination of primary antibodies consisted of mouse anti-E-cadherin clone 36 (1:20 000; BD Biosciences, San Jose, CA, USA; 610182), mouse anti-pan-cytokeratin (C-11; 1:4000; Abcam; ab7753), and mouse anti-pan-cytokeratin clone AE1/AE3 (1:2000; Thermo Fisher Scientific, Rockford, IL, USA; MA5-13156). Finally, nuclei were stained with 4',6-diamidino-2-phenylindole (DAPI) and mounted with Prolong Diamond Antifade Mountant (ThermoFisher).

Imaging

Imaging was performed with the Vectra 3 system (PerkinElmer). A whole slide scan was first acquired at $\times 10$ magnification for TMA core annotation and region selection for multispectral imaging, which was performed in Phenochart software (PerkinElmer). Four multispectral images, stitched together, at $\times 20$ magnification were needed to cover each TMA core. All five filter cubes in the system were used for multispectral imaging, and the saturation protection feature was enabled. The signal intensities for each marker were later normalized for exposure, and spectral unmixing was performed by the use of inForm software (PerkinElmer) with spectral libraries of each fluorophore.

Image analysis

Initial image analysis was performed with PerkinElmer inForm Analysis software. Each scanned image was

visually examined by a pathologist (A.M. and P.M.), and regions/samples with staining artefacts and with large necrotic areas were excluded.

Image processing comprised the following steps: training session and image analysis session. The training session included manual annotation of three distinct types of region (tumour, stroma, and blank areas) performed by a pathologist on five images (training set). A machine-learning algorithm built into the inForm software was used to create the tissue segmentation algorithm.

Cell segmentation was performed on the basis of the nuclear DAPI staining. Nuclear marker expression (FOXP3) was evaluated in the DAPI-defined nuclear areas. Although the lymphocyte cytoplasm size can vary substantially, in the current study we observed predominant expression of the cytoplasmic/membranous markers (CD4, CD8, CD20, and CD45RO) in the 6-pixel (3- μ m) perinuclear zone. Therefore, for image analysis, the perinuclear area with a size of 6 pixels was considered to be the cell cytoplasm zone. In cases in which the distance between neighbouring cell nuclei was less than 6+6 pixels, an inForm built-in function corrected the cytoplasm segmentation by local reduction of the cytoplasm area, to prevent the overlap. These cytoplasm regions were used to evaluate expression of the CD4, CD8, CD20, CD45RO, and pan-cytokeratin/E-cadherin. *x* and *y* coordinates for each individual cell were retrieved.

Thresholding

The expression levels of the markers were used to classify cells into the three main subsets (immune cells, tumour cells, and marker-negative cells). Density plots of the protein expression of each marker were used to set the thresholds for 'marker-negative' and 'marker-positive' cells. Because the cytokeratin (CK) signal may focally overlap with immune cells that infiltrate tumour cell nests, cells simultaneously showing high immune marker expression and some CK expression were considered to be immune cells.

Data processing and statistical analyses

Subsequent data analysis and statistical analysis were performed with R software, version 3.3.3 (R Foundation for Statistical Computing, Vienna, Austria) and integrated development environment RStudio, version 1.0.143 (RStudio Team, Boston, MA, USA), with the following packages: gdata, ggplot, corplot, PerformanceAnalytics, scales, rms, survival, made4, reshape, and plyr.

Results

Comparison between multiplex and single-marker staining

Spectral unmixing was utilized for the detection and separation of the seven different fluorescent

signals (CD4, CD8, CD20, CD45RO, FOXP3, E-cadherin/pan-cytokeratin, and DAPI) in each of 57 NSCLC tissue samples (see example in Figure 1A1, B1). These images were then used to generate six single-marker pseudo-brightfield pictures in which individual marker signals were converted into 3,3'-diaminobenzidine (DAB)-like colour. The DAPI signal was used to visualize the cell nuclei (Figure 1A2; upper panel; Figure 1B2). Visual comparison of the conventional immunohistochemical staining showed good concordance with the corresponding unmixed multispectral images (Figure 1A2, lower panel).

To investigate immune cell infiltration in stromal and tumour regions separately, a proprietary machine-learning algorithm built into the inForm software was used to define three area types in the analysed images: tumour tissue (cancer cell mass), stromal regions, and blank areas (Figure 1B1, right panel). For visualization purposes, inForm was also used to visualize cell classes (Figure 1B1, middle and right panels); however, this classification was not used in further analysis.

Validation of multispectral imaging and spectral unmixing algorithm

Individual cells were identified by DAPI staining. Immune marker and CK expression levels were then used to classify all cells into the three main subsets: epithelial cells or cancer cells (high CK expression; low immune marker expression), immune cells (high expression of at least one of the five immune markers used in the study), and 'other' cells (low CK and immune marker expression) (supplementary material, Figure S1).

Next, we computed the quantity of single immune marker-positive cells in each sample, and normalized these values to the total cell counts separately in the total area, tumour compartment, and stromal compartment (Figure 2A). These digitally generated data were compared with the results of conventionally scored immune cell infiltrates in the single-stained tissue sections. Strong positive correlations for both the total tissue area and for the tumour and stromal compartments were demonstrated (Spearman $r=0.52-0.90$, $P<0.001$ for total area; supplementary material, Figure S2). Finally, both annotations, digital and conventional, were compared with RNAseq data, which were available for 35 of the tissue samples. The digital method yielded significant positive correlations for all five immune markers (Spearman $r=0.35-0.65$; supplementary material, Figure S2). The correlation of RNAseq-derived values with conventional visual scoring was weaker (Spearman $r=0.38-0.58$; supplementary material, Figure S2). Together, these data demonstrated high concordance with the classic scoring approaches or RNA analysis of the automated scoring system.

Subpopulations of immune cells

Next, we aimed to identify the predominant phenotypes of immune cells present in clinical NSCLC tissue samples. The cases were hierarchically clustered according to the mean expression levels of the main five immune markers separately in the total area, stromal region, and tumour region (supplementary material, Figures S3 and S4). Five main groups could be distinguished in the total area and in the stromal area, defined by: (1) high CD8 cell counts, average CD4 and CD20 cell counts, but low cell counts of all other markers; (2) by high CD8 cell counts but low cell counts of all other markers; (3) by FOXP3 infiltration; (4) high CD4 cell counts with or without CD8 cell infiltration and low cell counts of the other markers; and (5) a few cases with high CD45RO cell infiltration. We also compared the abundance of marker-positive cells between the two largest morphological tumour classes in NSCLC: adenocarcinoma ($n=28$) and squamous cell carcinoma ($n=22$). No statistically significant difference was found (data not shown).

When immune cells were clustered according to marker expression in a case-independent manner (supplementary material, Figure S5A, B), several double marker-positive or multimarker-positive immune cell subsets were identified. Consequently, the individual cell marker coexpression signatures were used to quantify specific immune cell subpopulations (supplementary material, Table S2) [39,40]. The abundance of different immune cell subpopulations is visualized in Figure 2B. The most abundant immune cell subpopulations in both regions were CD4 effector cells (CD4_Eff cells, single CD4⁺) and CD8 cytotoxic cells (CD8_Eff cells, single CD8⁺), followed by B cells (single CD20⁺). The fourth most abundant subtype was represented by CD4⁺FOXP3⁺CD45RO⁻ cells, also referred to as CD4 regulatory T naive cells (CD4_Treg_naive cells). Interestingly, CD4 activated regulatory T cells (FOXP3⁺CD45RO⁺) were only rarely seen. In general, we observed concordant infiltration of different immune cell types (supplementary material, Table S3).

Associations between immune infiltration, clinicopathological characteristics, and survival

The multiplex staining and digital image analysis resulted in a data matrix consisting of nine immune cell subtypes in two different tissue compartments. These immune profiles were used in an explorative analysis for associations with clinical parameters. Tumour cases were dichotomized into 'low' and 'high' subgroups according to the amount of each defined immune cell type (cut-off median). We then performed survival analysis with univariate Cox regression models, and visualized patient survival rates with Kaplan–Meier plots (supplementary material, Figure S6). Despite the absence of statistically significant associations, the general trends linked higher immune cell abundance with longer survival. Strongest trends were observed for

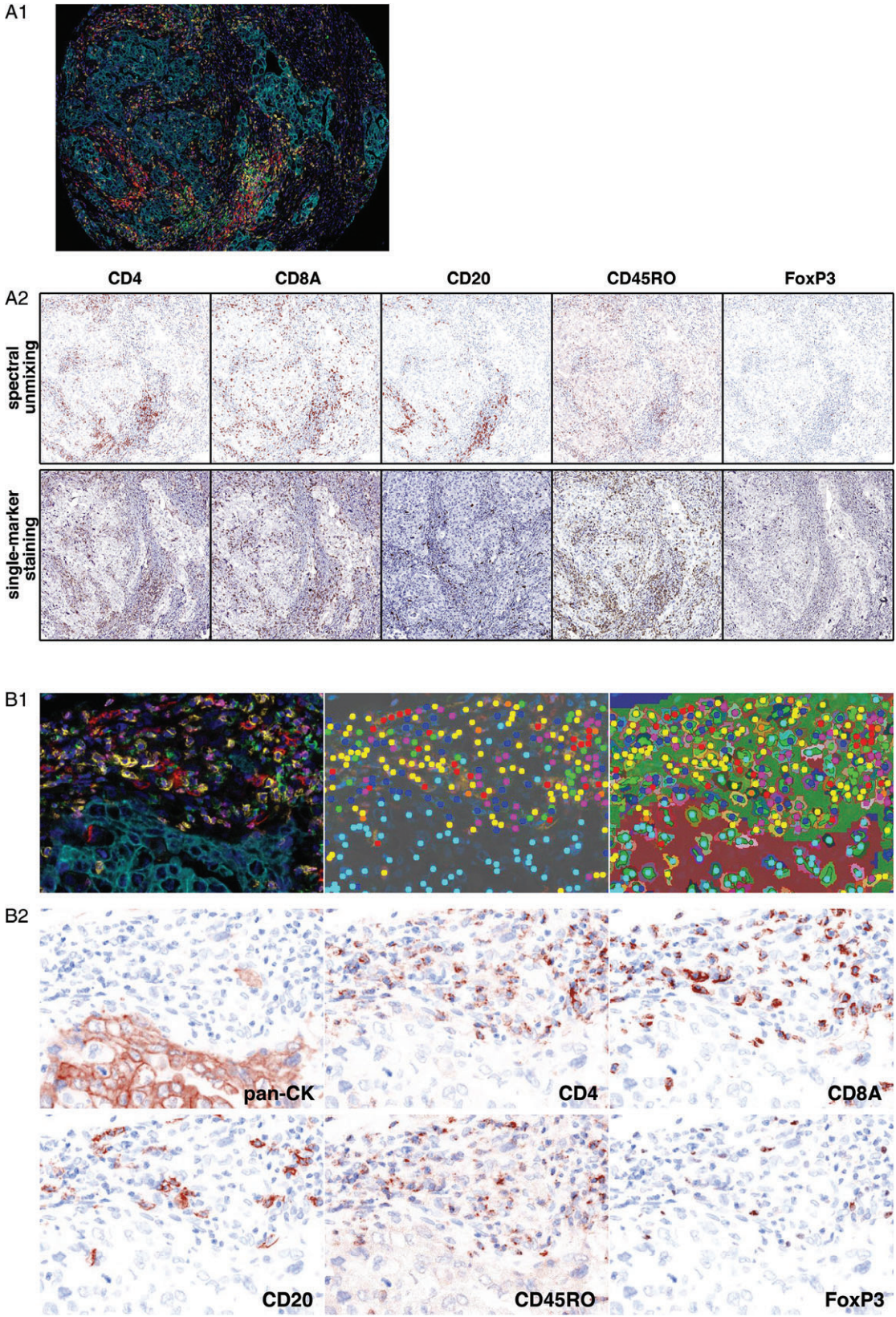


Figure 1. Multiplex seven-colour staining and analysis of human NSCLC. (A1) Multiplexed staining followed by multispectral imaging of a representative TMA core. (A2) Selected region of this core after spectral unmixing and conversion to a pseudo-DAB/haematoxylin appearance (upper panel) and single marker immunohistochemical staining, performed on the same tissue region on sequential sections (lower panel). (B1) Representative illustration displaying a high-magnification tissue region after multiplex staining and multispectral imaging (left image); cell phenotype automatic classification (middle panel) based on inForm built-in machine-learning algorithms; stromal (green), tumour (red) and blank (blue) regions classification (right image). (B2) Same region after spectral unmixing and conversion to a pseudo-DAB/haematoxylin appearance.

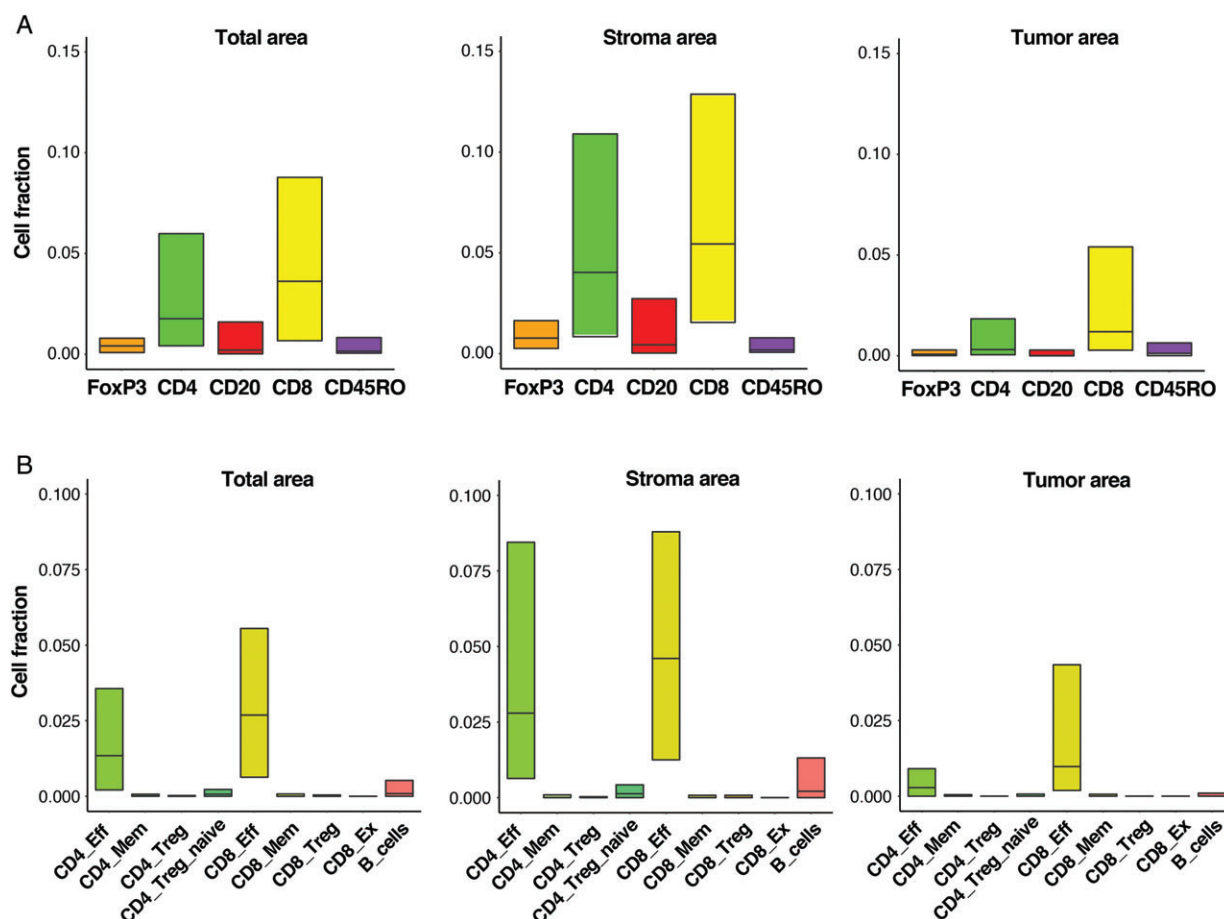


Figure 2. Infiltration of T-cell subpopulations in NSCLC tissue. (A) Quantity of marker-positive cells normalized to total cell numbers, calculated for each case in the total area, the stromal area, and the tumour area. Immune marker-negative cell class and tumour cells are not shown. Boxes represent first and third quartiles, and horizontal lines indicate the median level of cell abundance in the 57 evaluated samples. (B) Quantity of immune cell subpopulations, normalized to non-tumour cell numbers, calculated for each case in the total area, the stromal area, and the tumour area. Immune marker-negative cell class is not shown. Boxes represent the first and third quartiles, and horizontal lines represent the median level of the cell abundance in the 57 evaluated samples.

CD8 memory cells (CD8_Mem cells) cells in the total area and in stromal regions.

Absolute immune cell count may not provide sufficient information about immune infiltrate functional status. To capture dynamic properties of the tumour–immune interplay, we compared the numbers of immune cells in the tumour and in the stromal compartment, as this could reflect the ability to infiltrate the tumour mass. The analysis demonstrated that cases with a higher intratumoural/stromal ratio of CD8_Eff cell infiltration were associated with improved survival (Figure 3A). A similar trend was observed for CD4_Eff cells, although it was not statistically significant (supplementary material, Figure S7A).

The ratio between (cytotoxic) CD8 cells and FOXP3 cells is associated with survival in breast cancer, melanoma, and colorectal cancer [41–44]. We thus examined the ratio between CD8_Eff cells and FOXP3-positive classic CD4 T-regulatory cells (CD4_Treg cells). As illustrated in Figure 3B and supplementary material, Figure S7B, the high CD8_Eff/CD4_Treg ratio was associated with improved survival, having a particularly strong impact when

analysed in the tumour compartment. The other regulatory immune cell subclass [CD8⁺FOXP3⁺ cells, CD8 T-regulatory cells (CD8_Treg cells)] showed similar results when they were related to the number of effector cells (CD8_Eff cells) in tumour compartments (Figure 3B; supplementary material, Figure S7B).

Spatial distribution of immune cells and survival

The digital image analysis enables us to exactly localize individual immune cells in the tissue, and subsequently determine the spatial distribution of each type of immune cell with respect to cancer cells. Using spatial coordinates for each cell, we computed the shortest distance from each of the immune cells to the nearest cancer cell. Density plots representing distributions of the immune-to-tumour cell distances are shown in Figure 4A. In general, immune cell quantity was maximal at a distance of approximately 15–30 μ m from tumour cells. It was observed however, that there was some variation between cell subpopulations. Thus, CD8_Eff and CD8_Mem cells had a distinct tendency to group at a distance of approximately 15–20 μ m, but, in contrast, B cells showed a quite even distribution pattern.

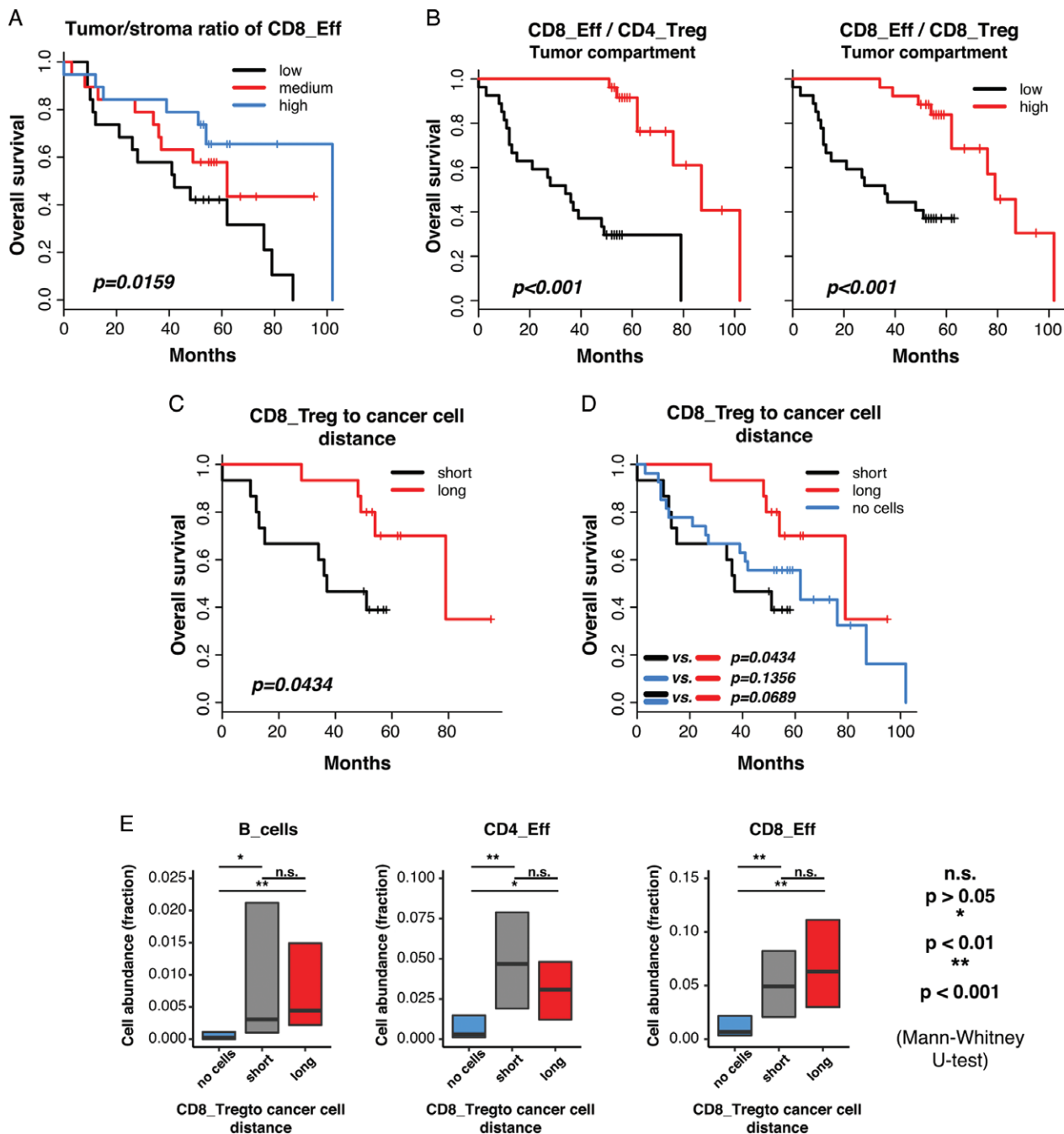


Figure 3. Survival analysis for selected immune metrics. (A) The Kaplan–Meier plot illustrates survival differences based on the ratio between intratumoural and stromal infiltration of CD8_Eff cells. (B) High ratios between CD8_Eff and CD4_Treg cells (left figure) and between CD8_Eff and CD8_Treg cells (right panel) in the tumour compartment are associated with longer survival. (C) A short distance of CD8_Treg cells to the closest neighbouring cancer cells is associated with poor survival. (D) Survival curves based on distances of CD8_Treg cells to cancer cells are shown, together with the survival curve of CD8_Treg-negative cases. (E) Quantity of B cells, CD4_Eff cells and CD8_Eff cells in the three different groups: short CD8_Treg-to-cancer cell distance group, long-distance group, and the group without CD8_Treg infiltration. Boxes represent the first and third quartiles, and horizontal lines represent median levels of cell abundance. n.s., not significant.

Median values of immune-to-tumour cell distances for each individual case were calculated (Figure 4B) and used to test potential survival associations. CD8_Treg cells showed a statistically significant adverse impact on survival in cases in which they were predominantly localized close to the tumour cells, with median distances of $<32 \mu\text{m}$ to tumour cells (37-month versus 79-month median survival for short and long distances respectively, hazard ratio = 3.39) (Figure 3C;

supplementary material, Figure S8). In this analysis, 27 cases could not be included because they lacked infiltrating CD8_Treg cells in their tissue samples. Interestingly, the mean 5-year survival of these patients was 43 months, thus approaching the mean 5-year survival of the short-distance CD8_Treg cases (39 months) in contrast to the long-distance CD8_Treg cases (56 months) (Figure 3D, left panel). We then computed the abundance of CD4_Eff cells, CD8_Eff

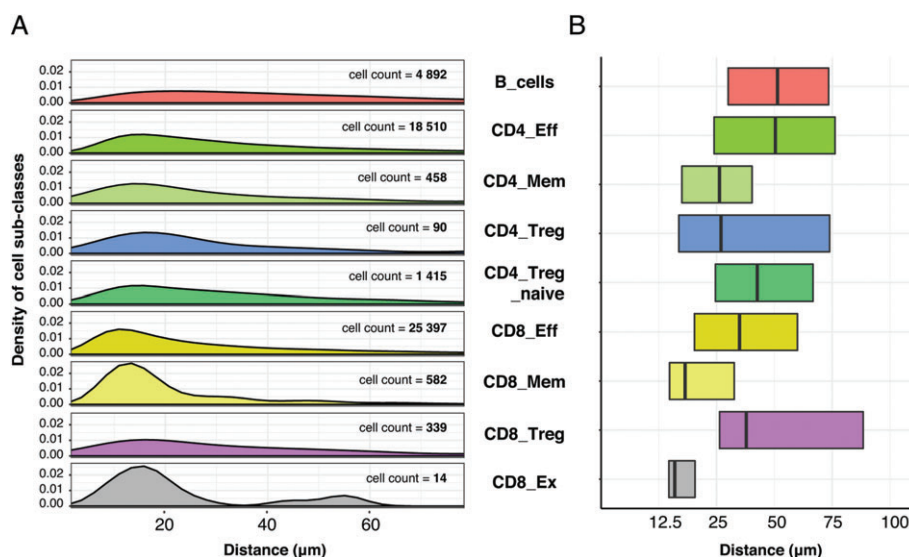


Figure 4. Immune cell distribution in relation to cancer cells. (A) Density plots demonstrating the distribution of the immune cells according to their distance from the nearest cancer cells. (B) Box-plots illustrating the case-wise distribution of the immune cells according to their distance from the nearest cancer cells, where boxes represent the first and third quartiles, and vertical lines indicate median levels of cell abundance.

cells and B cells in three CD8_Treg distance groups: the long-distance group, the short-distance group, and the no cell group. Interestingly, there was no statistically significant difference in immune cell abundance between the long-distance and short-distance groups, but the CD8_Treg-negative group was characterized by significantly lower immune cell abundance (Figure 3D, right panel).

Discussion

The success of the newly introduced checkpoint inhibitors has fundamentally changed the perspective of oncologists and cancer researchers on the process of tumourigenesis and the possibility of curing cancer. Tremendous efforts have been made to understand the immune reaction in the context of therapy, but also to better understand cancer immunity in the natural course of the disease. The most advanced immune-based prognostic system is the Immunoscore in colorectal cancer, where the assessment is based on the cell density of CD3⁺ and CD8⁺ cells in the tumour center and at the invasive margin [45]. The prognostic impact independently from tumour stage was validated in multiple independent cohorts, and has now been evaluated in a multinational prognostic trial [46]. The situation in lung cancer seems to be more difficult than that in colorectal cancer, for which an immune score has already been established.

A number of previous studies have analysed immune cell infiltrates in lung cancer, mostly using traditional immunohistochemical approaches on serial sections, with a preference for CD4 [47,48] and CD8 T-lymphocyte subsets [47,49], and less frequently other lymphocyte subsets, including B cells [20], FOXP3

cells [50] and CD45RO cells [51]. The prognostic data from these studies are not consistent, and seldom reach significance when multiple testing is performed [52]. Several other immune cell subsets have also been suggested to be of prognostic relevance, such as CD20 cells, plasma cells [20], macrophage subtypes [53], and natural killer cells [54].

Thus, in lung cancer, it is still unclear which cell types, along with their locations, are most important for tumourigenesis and will best predict survival or response to immunotherapy. In this situation, the strategy of combining multiplex markers with automated spatial cell annotation seems to be a very attractive tool with which to elucidate the multifaceted immune profiles in lung cancer. Consequently, we evaluated such a multiplex technique with digital image analysis to describe the immune infiltrates in NSCLC, and were able to show that the method produced reliable data that allowed quantification and localization of important subtypes of immune cells in their natural environment. We observed heterogeneous lymphocyte populations in the tumour microenvironment, with a predominance of cytotoxic T cells (CD8_Eff cells), CD4_Eff cells, and B cells. A higher abundance of different lymphocyte subtypes suggested improved survival. However, statistical significance was not reached in these tests, most probably because of the relatively low number of cases.

Although the total number of cytotoxic T cells did not show a significant prognostic impact, the ratio between cytotoxic T cells in the tumour and stromal compartments, i.e. the proportion of cells that migrate into the tumour nests, were associated with longer survival. This ratio may give an estimate of the ability of cytotoxic immune cells to migrate into the tumour mass and to exert their functions. In addition, we were able to show that the interplay between regulatory T-cell and

T effector cells, measured as a ratio of cell number in each compartment, has a strong impact on survival. The impact of this basic T-effector/T-regulatory cell ratio has been described in other cancer types [41–44], but, to our knowledge, hitherto not in NSCLC. This ratio may serve as an estimate of the antitumour immunity activation/inhibition status.

Accumulating evidence demonstrates the importance of the spatial features of the immune infiltrate. Thus, Nagl *et al* observed a prognostic capacity of the deviations from randomly predicted distances between CD20 and FOXP3 cells in anal squamous cell carcinoma [55]. Berthel *et al* reported complex infiltration patterns of CD3⁺ and CD163⁺ cells in colorectal cancer liver metastases, which was also linked to survival outcome [56]. Finally, in a study by Carstens *et al*, a technique similar to this study's was used to analyse pancreatic cancer. It was shown that cytotoxic T-cell accumulation in the immediate vicinity of cancer cells is correlated with increased survival [57].

Here, we demonstrated that accumulation of CD8 regulatory cells in the immediate vicinity of tumour cells was associated with significantly shorter survival. CD8 regulatory cells in our study were identified by the coexpression of CD8 and FOXP3. CD8⁺FOXP3⁺ T-regulatory cells have been described in colon [58], prostate [59] and breast cancers [60], and have been reported to have an immunosuppressive nature. We therefore hypothesize that accumulation of CD8 regulatory cells near tumour cells form a functional barrier, which blocks antitumour immunity, presumably through modulation of the immune checkpoint machinery. This hypothesis is also supported by the analysis of immune-low cases, which, in our study, showed survival rates similar to those of cases with peritumoural CD8_{Treg} accumulation.

Despite the overall reliability of the data produced by multispectral imaging, some limitations should be mentioned. We observed some degree of crosstalk between a couple of the fluorophores with overlapping emission spectra. Multispectral unmixing of fluorescent signals is sensitive to variations in the signal profile of the emitting fluorophores, which may be slightly altered when staining becomes very intense (personal communication, PerkinElmer). For example, in our dataset we identified a cell subset with CD20 and CD8 coexpression, which was due to this issue. This subset was excluded from further analysis in the current study. Such an approach may, however, lead to a certain degree of data loss. This can be resolved in future studies by ensuring that no cells are stained above a certain threshold. Moreover, it should be noted that our results are based on only a relatively small cohort of 57 NSCLC patients. Thus, the results have to be regarded as descriptive, and should be validated in a larger dataset.

In conclusion, we validated a multiplex imaging system for use on diagnostic tissue samples. The technique enabled us to provide an immune cell-based classification of NSCLC, including an *in situ* map with spatial cell distribution. The particular prognostic impacts of

different constellations of immune cell infiltrates underline the value of this multiplex strategy. We believe that this technique may qualify to be part of the routine characterization of the immune status of individual cancer patients.

Acknowledgements

PM receives support from the Swedish Cancer Society (Cancerfonden Lions Cancerfonden).

Author contributions statement

AM designed the study, performed visual quantification, analysed data, performed statistical analysis, and wrote the manuscript. CHB performed sample staining and scanning, and contributed to the writing and preparation of the manuscript. MB performed visual quantification, analysed data, and contributed to the writing and preparation of the manuscript. DD performed RNAseq analysis, and contributed to the writing and preparation of the manuscript. TS contributed to the acquisition, analysis and interpretation of data, and contributed to the writing of the manuscript. JB contributed to the acquisition, analysis and interpretation of data, and contributed to the writing of the manuscript. PM analysed and displayed the data, wrote the manuscript, and contributed to designing the study. All authors approved the manuscript and agreed with its submission.

References

1. Larkin J, Chiarion-Sileni V, Gonzalez R, *et al*. Combined nivolumab and ipilimumab or monotherapy in untreated melanoma. *N Engl J Med* 2015; **373**: 23–34.
2. Rosenberg JE, Hoffman-Censits J, Powles T, *et al*. Atezolizumab in patients with locally advanced and metastatic urothelial carcinoma who have progressed following treatment with platinum-based chemotherapy: a single-arm, multicentre, phase 2 trial. *Lancet* 2016; **387**: 1909–1920.
3. Bauml J, Seiwert TY, Pfister DG, *et al*. Pembrolizumab for platinum- and cetuximab-refractory head and neck cancer: results from a single-arm, phase II study. *J Clin Oncol* 2017; **35**: 1542–1549.
4. Eggermont A, Robert C, Soria JC, *et al*. Harnessing the immune system to provide long-term survival in patients with melanoma and other solid tumors. *Oncoimmunology* 2014; **3**: e27560.
5. Le DT, Uram JN, Wang H, *et al*. PD-1 blockade in tumors with mismatch-repair deficiency. *N Engl J Med* 2015; **372**: 2509–2520.
6. Sharma P, Allison JP. The future of immune checkpoint therapy. *Science* 2015; **348**: 56–61.
7. Whiteside TL, Demaria S, Rodriguez-Ruiz ME, *et al*. Emerging opportunities and challenges in cancer immunotherapy. *Clin Cancer Res* 2016; **22**: 1845–1855.
8. Lu L, Barbi J, Pan F. The regulation of immune tolerance by FOXP3. *Nat Rev Immunol* 2017; **17**: 703–717.
9. Boussiotis VA. Molecular and biochemical aspects of the PD-1 checkpoint pathway. *N Engl J Med* 2016; **375**: 1767–1778.
10. Dong ZY, Wu SP, Liao RQ, *et al*. Potential biomarker for checkpoint blockade immunotherapy and treatment strategy. *Tumour Biol* 2016; **37**: 4251–4261.

11. Bosmuller H, Haitchi-Petnehazy S, Webersinke G, *et al.* Intratumoral lymphocyte density in serous ovarian carcinoma is superior to ERCC1 expression for predicting response to platinum-based therapy. *Virchows Arch* 2011; **459**: 183–191.
12. Gibney GT, Weiner LM, Atkins MB. Predictive biomarkers for checkpoint inhibitor-based immunotherapy. *Lancet Oncol* 2016; **17**: e542–e551.
13. Brunnstrom H, Johansson A, Westbom-Fremer S, *et al.* PD-L1 immunohistochemistry in clinical diagnostics of lung cancer: inter-pathologist variability is higher than assay variability. *Mod Pathol* 2017; **30**: 1411–1421.
14. Jacquelot N, Roberti MP, Enot DP, *et al.* Predictors of responses to immune checkpoint blockade in advanced melanoma. *Nat Commun* 2017; **8**: 592.
15. Geissler K, Fornara P, Lautenschlager C, *et al.* Immune signature of tumor infiltrating immune cells in renal cancer. *Oncoimmunology* 2015; **4**: e985082.
16. Fridman WH, Galon J, Pages F, *et al.* Prognostic and predictive impact of intra- and peritumoral immune infiltrates. *Cancer Res* 2011; **71**: 5601–5605.
17. Matsumoto H, Koo SL, Dent R, *et al.* Role of inflammatory infiltrates in triple negative breast cancer. *J Clin Pathol* 2015; **68**: 506–510.
18. Bienkowski M, Preusser M. Prognostic role of tumour-infiltrating inflammatory cells in brain tumours: literature review. *Curr Opin Neurol* 2015; **28**: 647–658.
19. Donnem T, Kilvaer TK, Andersen S, *et al.* Strategies for clinical implementation of TNM-Immunoscore in resected nonsmall-cell lung cancer. *Ann Oncol* 2016; **27**: 225–232.
20. Lohr M, Edlund K, Botling J, *et al.* The prognostic relevance of tumour-infiltrating plasma cells and immunoglobulin kappa C indicates an important role of the humoral immune response in non-small cell lung cancer. *Cancer Lett* 2013; **333**: 222–228.
21. Schmidt M, Hellwig B, Hammad S, *et al.* A comprehensive analysis of human gene expression profiles identifies stromal immunoglobulin kappa C as a compatible prognostic marker in human solid tumors. *Clin Cancer Res* 2012; **18**: 2695–2703.
22. Hennequin A, Derangere V, Boidot R, *et al.* Tumor infiltration by Tbet+ effector T cells and CD20+ B cells is associated with survival in gastric cancer patients. *Oncoimmunology* 2016; **5**: e1054598.
23. Mlecnik B, Tosolini M, Kirilovsky A, *et al.* Histopathologic-based prognostic factors of colorectal cancers are associated with the state of the local immune reaction. *J Clin Oncol* 2011; **29**: 610–618.
24. Mlecnik B, Bindea G, Angell HK, *et al.* Integrative analyses of colorectal cancer show Immunoscore is a stronger predictor of patient survival than microsatellite instability. *Immunity* 2016; **44**: 698–711.
25. Ono M, Tsuda H, Shimizu C, *et al.* Tumor-infiltrating lymphocytes are correlated with response to neoadjuvant chemotherapy in triple-negative breast cancer. *Breast Cancer Res Treat* 2012; **132**: 793–805.
26. Denkert C, von Minckwitz G, Brase JC, *et al.* Tumor-infiltrating lymphocytes and response to neoadjuvant chemotherapy with or without carboplatin in human epidermal growth factor receptor 2-positive and triple-negative primary breast cancers. *J Clin Oncol* 2015; **33**: 983–991.
27. Ladoire S, Enot D, Andre F, *et al.* Immunogenic cell death-related biomarkers: impact on the survival of breast cancer patients after adjuvant chemotherapy. *Oncoimmunology* 2016; **5**: e1082706.
28. Ngiew SF, Young A, Jacquelot N, *et al.* A Threshold level of intra-tumor CD8+ T-cell PD1 expression dictates therapeutic response to anti-PD1. *Cancer Res* 2015; **75**: 3800–3811.
29. Zito Marino F, Ascierto PA, Rossi G, *et al.* Are tumor-infiltrating lymphocytes protagonists or background actors in patient selection for cancer immunotherapy? *Expert Opin Biol Ther* 2017; **17**: 735–746.
30. Prat A, Navarro A, Pare L, *et al.* Immune-related gene expression profiling after PD-1 blockade in non-small cell lung carcinoma, head and neck squamous cell carcinoma, and melanoma. *Cancer Res* 2017; **77**: 3540–3550.
31. O'Hurley G, Sjostedt E, Rahman A, *et al.* Garbage in, garbage out: a critical evaluation of strategies used for validation of immunohistochemical biomarkers. *Mol Oncol* 2014; **8**: 783–798.
32. Micke P, Mattsson JS, Djureinovic D, *et al.* The impact of the fourth edition of the WHO classification of lung tumours on histological classification of resected pulmonary NSCCs. *J Thorac Oncol* 2016; **11**: 862–872.
33. Mattsson JS, Brunnstrom H, Jabs V, *et al.* Inconsistent results in the analysis of ALK rearrangements in non-small cell lung cancer. *BMC Cancer* 2016; **16**: 603.
34. Djureinovic D, Hallstrom BM, Horie M, *et al.* Profiling cancer testis antigens in non-small-cell lung cancer. *JCI Insight* 2016; **1**: e86837.
35. Flicek P, Amode MR, Barrell D, *et al.* Ensembl 2012. *Nucleic Acids Res* 2012; **40**: D84–D90.
36. Trapnell C, Williams BA, Pertea G, *et al.* Transcript assembly and quantification by RNA-Seq reveals unannotated transcripts and isoform switching during cell differentiation. *Nat Biotechnol* 2010; **28**: 511–515.
37. Liao Y, Smyth GK, Shi W. FeatureCounts: an efficient general purpose program for assigning sequence reads to genomic features. *Bioinformatics* 2014; **30**: 923–930.
38. Tóth ZE, Mezey É. Simultaneous visualization of multiple antigens with tyramide signal amplification using antibodies from the same species. *J Histochem Cytochem* 2007; **55**: 545–554.
39. Reiser J, Banerjee A. Effector, memory, and dysfunctional CD8(+) T cell fates in the antitumor immune response. *J Immunol Res* 2016; **2016**: 8941260.
40. Sakaguchi S, Miyara M, Costantino CM, *et al.* FOXP3+ regulatory T cells in the human immune system. *Nat Rev Immunol* 2010; **10**: 490–500.
41. Semeraro M, Adam J, Stoll G, *et al.* The ratio of CD8+/FOXP3 T lymphocytes infiltrating breast tissues predicts the relapse of ductal carcinoma in situ. *Oncoimmunology* 2016; **5**: e1218106.
42. Ladoire S, Senovilla L, Enot D, *et al.* Biomarkers of immunogenic stress in metastases from melanoma patients: correlations with the immune infiltrate. *Oncoimmunology* 2016; **5**: e1160193.
43. Asano Y, Kashiwagi S, Goto W, *et al.* Tumour-infiltrating CD8 to FOXP3 lymphocyte ratio in predicting treatment responses to neoadjuvant chemotherapy of aggressive breast cancer. *Br J Surg* 2016; **103**: 845–854.
44. Zeestraten EC, Van Hoesel AQ, Speetjens FM, *et al.* FoxP3- and CD8-positive infiltrating immune cells together determine clinical outcome in colorectal cancer. *Cancer Microenvironment* 2013; **6**: 31–39.
45. Galon J, Pages F, Marincola FM, *et al.* Cancer classification using the Immunoscore: a worldwide task force. *J Transl Med* 2012; **10**: 205.
46. Galon J, Mlecnik B, Marliot F, *et al.* Validation of the Immunoscore (IM) as a prognostic marker in stage I/II/III colon cancer: results of a worldwide consortium-based analysis of 1,336 patients. *J Clin Oncol* 2016; **34**: Abstract 3500.
47. Hiraoka K, Miyamoto M, Cho Y, *et al.* Concurrent infiltration by CD8+ T cells and CD4+ T cells is a favourable prognostic factor in non-small-cell lung carcinoma. *Br J Cancer* 2006; **94**: 275–280.
48. Wakabayashi O, Yamazaki K, Oizumi S, *et al.* CD4+ T cells in cancer stroma, not CD8+ T cells in cancer cell nests, are associated with favorable prognosis in human non-small cell lung cancers. *Cancer Sci* 2003; **94**: 1003–1009.

49. Kawai O, Ishii G, Kubota K, *et al.* Predominant infiltration of macrophages and CD8(+) T cells in cancer nests is a significant predictor of survival in stage IV nonsmall cell lung cancer. *Cancer* 2008; **113**: 1387–1395.
50. Kinoshita T, Muramatsu R, Fujita T, *et al.* Prognostic value of tumor-infiltrating lymphocytes differs depending on histological type and smoking habit in completely resected non-small-cell lung cancer. *Ann Oncol* 2016; **27**: 2117–2123.
51. Paulsen EE, Kilvaer T, Khanehenari MR, *et al.* CD45RO(+) memory T lymphocytes – a candidate marker for TNM-Immunoscore in squamous non-small cell lung cancer. *Neoplasia* 2015; **17**: 839–848.
52. Zeng DQ, Yu YF, Ou QY, *et al.* Prognostic and predictive value of tumor-infiltrating lymphocytes for clinical therapeutic research in patients with non-small cell lung cancer. *Oncotarget* 2016; **7**: 13765–13781.
53. Sun BS, Pei BX, Zhang K, *et al.* Significance of interstitial tumor-associated macrophages in the progression of lung adenocarcinoma. *Oncol Lett* 2016; **12**: 4467–4476.
54. Fend L, Rusakiewicz S, Adam J, *et al.* Prognostic impact of the expression of NCR1 and NCR3 NK cell receptors and PD-L1 on advanced non-small cell lung cancer. *Oncoimmunology* 2017; **6**: e1163456.
55. Nagl S, Haas M, Lahmer G, *et al.* Cell-to-cell distances between tumor-infiltrating inflammatory cells have the potential to distinguish functionally active from suppressed inflammatory cells. *Oncoimmunology* 2016; **5**: e1127494.
56. Berthel A, Zoernig I, Valous NA, *et al.* Detailed resolution analysis reveals spatial T cell heterogeneity in the invasive margin of colorectal cancer liver metastases associated with improved survival. *Oncoimmunology* 2017; **6**: e1286436.
57. Carstens JL, Correa de Sampaio P, Yang D, *et al.* Spatial computation of intratumoral T cells correlates with survival of patients with pancreatic cancer. *Nat Commun* 2017; **8**: 15095.
58. Chaput N, Louafi S, Bardier A, *et al.* Identification of CD8+CD25+Foxp3+ suppressive T cells in colorectal cancer tissue. *Gut* 2009; **58**: 520–529.
59. Kuniwa Y, Miyahara Y, Wang HY, *et al.* CD8+ Foxp3+ regulatory T cells mediate immunosuppression in prostate cancer. *Clin Cancer Res* 2007; **13**: 6947–6958.
60. Chakraborty S, Panda AK, Bose S, *et al.* Transcriptional regulation of FOXP3 requires integrated activation of both promoter and CNS regions in tumor-induced CD8+ Treg cells. *Sci Rep* 2017; **7**: 1628.

SUPPLEMENTARY MATERIAL ONLINE

Supplementary figure legends

Figure S1. Pan-cytokeratin expression in the analyzed cohort

Figure S2. Comparison between three different techniques to quantify immune markers

Figure S3. Clustering analysis of NSCLC cases based on immune cell profiles of the total area

Figure S4. Clustering analysis of NSCLC cases based on immune cell profiles in stroma and tumor compartment

Figure S5. Immune cell clustering analysis identified multi-marker-positive cell subpopulations

Figure S6. Immune cell infiltration and survival in NSCLC

Figure S7. Immune cell spatial distribution and survival in NSCLC

Figure S8. Immune cell-to-cancer cell distances and relation to patient survival

Table S1. Baseline clinicopathological data of the actual study cohort

Table S2. Immune cell subpopulations

Table S3. Correlation between different immune cell subpopulations